Journal of Volcanology and Geothermal Research 472 (2026) 108553

Contents lists available at ScienceDirect

Journal of Volcanology and Geothermal Research

journal homepage: www.journals.elsevier.com/journal-of-volcanology-and-geothermal-research

The application of InSAR DEMs for volcanic hazard assessments at Mount Taranaki, New Zealand

Samuel McGowan *, Jonathan Procter, Stuart Mead, Gabor Kereszturi

Volcanic Risk Solutions, Institute of Agriculture and Environment, Massey University, Private Bag 11222, Palmerston North, 4442, New Zealand

ARTICLE INFO

Keywords:
InSAR
DEM
Sentinel-1
Mass flow simulations

ABSTRACT

Interferometric Synthetic Aperture Radar (InSAR) can be used to detect ground motion but also processed further to generate Digital Elevation Models (DEMS). Sentinel-1 images are acquired continuously, and data is made available free of access in near real time making it a valuable tool for Earth observation and volcanic hazard assessment. Mass flow simulations require up to date DEMs for the results to be integrated in volcanic hazard management and mitigation. This study investigates the applicability of InSAR generated terrains as information and data with respect to volcanic hazard analysis as well as the input data in simulating block-and-ash flows (BAFs) following the collapse of volcanic domes on Mount Taranaki, New Zealand, using the Titan2D simulation toolkit. Results show that the accuracy of Sentinel-1 InSAR generated DEMs are limited for volcanic hazard analysis in areas of dense vegetation and steep topography due to temporal decorrelation and geometrical distortions. Together, these conditions introduce major differences in inundation extent and thickness distribution of simulated flows yet can provide some indication of flow impact which may be of relevance for rapid decision making in response to rapidly changing volcanic landscapes.

1. Introduction

Volcanic activity, and other natural hazards can cause serious damage to human society if no mitigation is taken (Holzer and Savage, 2013; Wilson et al., 2014). Remote sensing plays a crucial role as it allows scientists to gather global and regional data, rapidly, without putting themselves in danger (Chien and Tanpipat, 2012), aiding emergency management decision-making. Remote sensing in hazard management generally combines optical and radar data acquired from instrumented aircrafts or satellites (Gao, 2023). Radar acquisitions are classified as active remote sensing as they generate their own signal and therefore do not require solar radiation (Hay, 2000). The main advantage of remotely sensed radar data comes from its cloud penetrating properties and ability to acquire data during the night offering continuous, accurate surveying in the case of an event (Pepe and Calò, 2017). With increasing spatial coverage and shorter revisit periods, radar equipped satellites offer global data access to remote places on Earth which may not be equipped with ground instrumentation to detect the impacts of volcanic activity (Pinel et al., 2014). Many hazards occur in areas where no surveying equipment are deployed or where weather conditions do not allow for optical (e.g., dense cloud coverage in tropical environments) or ground observation or surveys (e.g., dense vegetation canopy). Active remote sensing therefore offers an efficient and cost-effective solution to regional and global monitoring.

Interferometric Synthetic Aperture Radar (InSAR) is an active remote sensing technique commonly used to study evolving processes such as surface deformation, based on the phase delay between pairs of radar images covering the same area (Zhou et al., 2009). In the case of volcanology, InSAR is commonly used pre-eruption to study surface deformation (Pallister et al., 2013) which may indicate an imminent eruption allowing decision makers to pre-emptively evacuate specific areas if required, or post-eruption to quantify volcanic induced change or the volume of material erupted (e.g., Albino et al., 2015) and for the spatial mapping of deposits (Dualeh et al., 2021; Ezquerro et al., 2023). InSAR has also been used to generate Digital Elevation Models (DEMs) of the Earth's surface such as the Shuttle Radar Topography Mission (SRTM, 30 m resolution) (Farr et al., 2007), the Global Digital Elevation Model (GDEM, 30 m resolution) (Tachikawa et al., 2011) and more recently a 12 m resolution DEM generated by the German satellite Tandem-X (European Space Agency- ESA). Outside these mapping campaigns, DEMs of areas of specific interest can be generated from pairs of SAR images acquired by orbiting satellites such as Sentinel-1, TerraSAR-X, TanDEM-X, PAZ. However, InSAR is yet to be tested or integrated into near real-time analysis for volcanic decision making due to the absence of freely accessible frequent and regular high-resolution acquisition beyond commercial options (e.g., 11 days for TanDEM-X

* Corresponding author.
E-mail address: s.mcgowan@massey.ac.nz (S. McGowan).

https://doi.org/10.1016/j.jvolgeores.2026.108553
Received 22 October 2025; Received in revised form 8 January 2026; Accepted 29 January 2026
Available online 6 February 2026

and TerraSAR-X as compared to the tasking of systems such as ICEYE with 6 h global revisit period) and due to differences in data accessibility policies. Efforts to increase high-resolution data accessibility free of charge have been made throughout the years with projects such as the Volcano Demonstrator launched by the Committee on Earth Observing Satellites (CEOS) in 2019 (Pritchard et al., 2021) and the Geohazard Supersites and Natural Laboratory initiative (GSNL) (Borges et al., 2023). However, these programs only cover specific hazardous volcanoes leaving many areas deprived of free, frequent high-resolution data. The Sentinel-1 constellation which has a revisit period of 6–12 days, offers a reliable open-source collection of SAR imagery, at the expense of a lower spatial resolution.

DEMs in volcanology are principally used to estimate volume changes in the case of an event by computing the elevation difference before and after a landscape changing event (Albino et al., 2020; Kubanek et al., 2015; Procter et al., 2010), but also for computational modelling of volcanic hazards such as lahars and mass flow simulations of collapsing volcanic edifices (Manville et al., 2013; Mead et al., 2016; Mead and Magill, 2017; Procter et al., 2014). Modelling of gravitational instabilities are necessary to delineate potentially affected areas and to build hazard maps based on the run-out distance and deposit inundation thickness over a terrain represented by an up-to-date DEM (Procter et al., 2009b; Stevens et al., 2003). The accuracy of the DEM will strongly influence the outcome of the simulations and is greatly dependent on slope angles, curvature and channel identification (Stefanescu et al., 2010; Viotto et al., 2023). Several studies across various volcanoes have evaluated the suitability and reliability of DEMs generated by various techniques for lahar and mass flow simulations: InSAR campaigns (e.g., SRTM, TOPSAR, GDEM, TanDEM-X) (e.g., Hubbard et al., 2007; Huggel et al., 2008; Deng et al., 2019; Viotto et al., 2023); photogrammetry (e.g., Andaru et al., 2022), Light Detection And Ranging (LiDAR) (e.g., Davila et al., 2007), contour line derived (e.g., Stevens et al., 2003; Davila et al., 2007; Muñoz-Salinas et al., 2009; Mead et al., 2016). Ground based and LiDAR generated DEMs are of higher resolution but are more expensive to deploy, cover a smaller area and are limited by meteorological conditions (Liu, 2008; Procter et al., 2014), offering a less-cost effective solution than satellite-based radar remote sensing. Sentinel-1 data is primarily designed to study deformation (e.g., Harvey, 2021), but nonetheless, several studies were successful in DEM generation or elevation extraction as summarized in the literature review of Braun (2021). This study aims to assess the suitability and reliability of InSAR generated DEMs from free, open-source Sentinel-1 data for debris flow modelling in the context of volcanic hazard assessment. As a case study, we use Titan2D to simulate a dome collapse at Mount Taranaki, New Zealand, using DEMs generated from Sentinel-1 and from a 1 m resolution LiDAR DEM generated by Land Information New Zealand (LINZ) in 2021 to use as a reference.

1.1. Area of study: Mount Taranaki, New Zealand

The North Island of New Zealand hosts a large stratovolcano, Mount Taranaki (2518 m). Despite not having erupted since ≈1800 AD (Platz et al., 2012), this volcano presently causes considerable mass flow hazards (Procter et al., 2021a). This volcano is the youngest of a 1.8 Ma NW-SE trending andesite volcanism lineament composed of Mount Pouakai (1400 m) and Mount Kaitake (682 m) (Fig. 1) (Zernack et al., 2009). These volcanoes are historically characterized by alternating periods of edifice growth and collapse generating block-and-ash flows (BAFs), highlighted by the current geomorphology of these edifices and the preserved stratigraphy in the surrounding ring plain (c.150 m^3) (Zernack, 2020). From preserved deposits, more than 14 unconfined volcanic debris avalanche deposits have been recorded within the last 210,000 years (Procter et al., 2021a; Zernack and Procter, 2020) with the most recent flank collapse occurring around 7500 years ago (Procter et al., 2021b). The Pungarehu Formation is the largest know failure produced with an estimated volume of 6–7.5 km^3 (Ui et al., 1986). It is estimated that one major slope failure occurs every 10,000–14,000 years (Zernack et al., 2011). More recent activity was recorded in 1999 and 2009 following heavy rain periods, remobilising unconsolidated volcanic material in the form of lahars (Procter et al., 2021b). The last 1000 years of volcanic activity has been dominated by <VEI 3–4 eruptions and associated BAF's primarily in the northern sectors of the volcano with the Stony-Hangatahua River being the main flow path and drainage (Lerner et al., 2019).

The steep slopes of this stratovolcano favour mass flows transported across several river catchments such as the Upper Stony-Hangatahua River (Fig. 1). This area of erosion and deposition is located on the northwestern side of Mount Taranaki and presents a considerable amount of threat to farming and human infrastructures settled in the ring plain (Fig. 1). A study carried out by Betts et al. (2010) identified that storm intensity may have been increasing since 1980, implying severe erosion and aggradation on Mount Taranaki, enhancing the hazard exposure to neighbouring communities. These lower magnitude, but much more frequent secondary(laharic) volcanic events, continuously shape the modern landscape but are considerably less impacting than large single volcanic debris avalanches and BAF's generated from eruptions and dome collapses (Zernack, 2020). The study of Procter et al. (2009a) simulated the latest dome collapses of Mount Taranaki (AD 1880s and AD 1755) which affected the NW flank, by adjusting iteratively the volume and physical properties of the initial pile material to match the run-out extent of BAFs (10 km from source) observed in the field. These simulations were performed using Titan2D, a code designed by the Geophysical Mass Flow Modelling Group, SUNY Buffalo, enabling the simulation of dry granular flows propagating over a selected DEM. Numerical modelling requires accurate DEMs as topography strongly controls downslope propagation of mass movements (Patra et al., 2005). In this study we perform Titan2D simulations using similar parameters defined by Procter et al. (2009a) for BAFs propagating over DEMs produced by Sentinel-1 interferometry to assess their reliability for debris flow modelling and hazard assessment.

2. Interferometry radar

InSAR is an active remote sensing system that allows us to map topographic elevation and surface deformation based on the phase delay of two radar images covering the same geographical area (Chen et al., 2000). Active remote sensing acquisitions are insensitive to lighting variations and can take place at any given time of the day, for any weather conditions making it a powerful tool for gathering data rapidly in the case of natural hazard emergency management (Pepe and Calò, 2017). In the context of volcanic applications, ground measurements and optical observations during an eruption are hazardous and often constrained by the visibility through ash clouds. For given wavelengths, radar acquisitions are also useful to study in overgrown areas such as forests as the emitted signal can penetrate the canopy surface to reach ground floor (Tsokas et al., 2022). The main wavelengths used for Earth's observation are X-band (λ=3 cm), C-band (λ=5 cm) and L-band (λ=23.5 cm), with longer wavelengths penetrating deeper through clouds and vegetation. These images are acquired by satellites (e.g., Sentinel-1, ALOS, Envisat, TerraSAR-X) that have a given orbit and revisit period. Sentinel-1 is a C-band operating satellite constellation (λ=5 cm) offering global and free SAR data, with a 6–12 day revisit period travelling along a near-polar orbit (Braun, 2021). The recorded phase in a radar image (φ) is a sum of different contributions (Ketelaar, 2009) (Eq. (1)) that need to be corrected for to retrieve true surface displacements or elevation models.

$$(\varphi) = (\varphi_f) + (\varphi_{topo}) + (\varphi_{disp}) + (\varphi_{atmo}) + (\varphi_{err}) \quad (1)$$

The flat Earth (φ_f) represents the phase shift due to Earth's curvature distorting the distances across the image and is corrected by flattening the image using the orbital parameters (Braun, 2021). The topographic

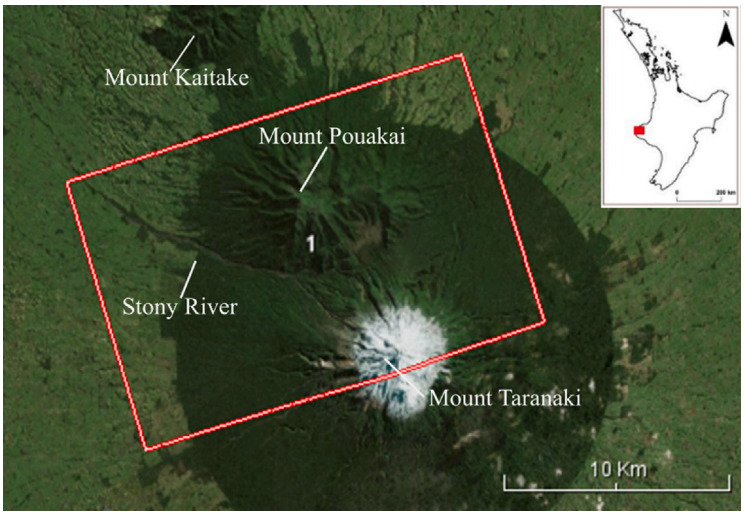

Fig. 1. Aerial image of Mount Taranaki. Red box indicates the spatial extent of area of interest. Inset show's location of Mount Taranaki in New Zealand.

noise (φ_{topo}) results from different look angles leading to a phase difference between two points that are not at the same altitude (Journeau et al., 2021) and is corrected using a DEM (Bemelmans et al., 2023). The displacement phase (φ_{disp}) relates to the loss of coherence between the two acquisitions due to evolving processes. Coherence (γ) refers to the magnitude of cross-correlation between two co-registered radar images, quantifying their degree of similarity on a scale of 0 to 1 (with 1 being 100% similar) (Joyce et al., 2009). Atmospheric noise (φ_{atmo}) arises from changes in pressure, temperature, and humidity between the acquisitions (Albino and Biggs, 2021; Zhao et al., 2021). The error phase (φ_{err}) regroups noise arising from orbital offsets and data processing.

Interferograms allow for a spatial representation of surface deformation and elevation change as repeating rainbow-coloured fringes. The initial data produces a wrapped signal ranging between 0 and 2π, due to the sinusoidal periodicity of the signal (Ferretti et al., 2007) and where each cycle represents half the sensor's wavelength. By adding the correct integer multiple of 2π to the fringes (Yu et al., 2019), the interferogram is unwrapped, producing a continuous field of phase change (Dzurisin, 2006). By removing the previously cited phase contributions, we can isolate true surface displacement or elevation values between the acquisition dates. In our case, we aim to retrieve (φ_{topo}), assuming no surface deformation has occurred between the two SAR images. The main limitation to InSAR usage is caused by its sensitivity to noise and phase decorrelation (Thiele et al., 2013). Interferograms can be accurately unwrapped if the signal-to-noise ratio is sufficient to distinguish clear fringes. Areas of decorrelation have a speckle effect displaying individual pixels of rainbow-colours in a randomly manner (Choi and Jeong, 2019). Noise can occur from the different phase contributors previously mentioned in Eq. (1), but can also occur from noise within the system (Woodhouse, 2005). This random additive noise generates unpredictable variation in amplitude and phase measurements. The ionosphere and troposphere are the main sources of atmospheric noise when using InSAR (Chaussard et al., 2016). C-band acquisitions are particularly sensitive to tropospheric delays caused by changes in temperature, pressure and more importantly water vapour (Chaussard et al., 2016). Decorrelation between SAR images is described either temporal or geometrical. Temporal decorrelation affects data acquired by repeat-pass interferometry due to the elapsed time between the SAR images. During this period, the surface image can change as soil gets wet or dries out, snow falls or melts, vegetations grows or is cropped, leaves fall off the branches (Bamler and Hartl, 1998). All these physical changes will impact the reflected signal and the measured coherence (Woodhouse, 2005). There are two sources of geometric decorrelation which arise from the baseline distance between the two acquisition (Chen et al., 2022) and the volumetric variations in target areas composed of vertical scatterers of different heights such as forests (Woodhouse, 2005). The forest is imaged from a slightly different angle which will affect the amount of penetrating signal and therefore the volumetric scattering. All these factors contribute to the quality of the produced interferogram, and therefore the data generated from it (Rosen et al., 2000). Areas that remain stable over time such as rock outcrops, roads and buildings are coherent and will not produce any decorrelation (Crosetto et al., 2016).

3. Methodology

3.1. Generating DEMs using SNAP

Our objective is to generate a Sentinel-1 radar database from 2015 up to present day of Mount Taranaki to assess the applicability of the DEMs generated using the SeNtinel Application Platform (SNAP). SNAP is a free and interactive software developed by the ESA to process satellite data can be downloaded from the Scientific Toolbox Exploitation Platform (STEP). We select pairs of Sentinel-1 images suitable for DEM generation using the Alaska Satellite Facility SBAS tool (Hogenson et al., 2020). Using image pairs with a short temporal baseline (B_T) is crucial to generating DEMs, especially in vegetated and aqueous areas, to avoid total loss of coherence (Ferretti et al., 2007). It is equally best suited to use image pairs at times of minimum vegetation cover which are acquired during dry periods, as water vapour in the atmosphere induces phase delays (Chaussard et al., 2016), decreasing the quality of the data. The perpendicular baseline ($B_\perp$), which refers to the distance between the satellites position at the time of the acquisition, should range between 150 and 300 m. Small perpendicular baseline values (< 30 m) are highly sensitive to noise and atmospheric effects (Ferretti et al., 2007), while very large baseline acquisitions lose coherence due to the difference in acquisition geometry (Ferretti et al., 2007). We select images with $B_\perp$ > 150 m, acquired between January and April of each year since 2015 (Table 1) to have minimum snow cover on the summit of the volcano and to reduce atmospheric delays (φ_{atmo}), as these months are the driest. We use data from both the ascending and descending orbit to compare the effect of topography and acquisition angle on DEM generation. The detailed methodology to generate DEMs from Sentinel-1 data using SNAP is highlighted in Fig. 2. A step by step tutorial is also available in Braun (2021) and should be referred to for detailed explanations. Final products are further analysed in QGIS.

To assess the accuracy of our InSAR generated DEMs, we use a 1 m Lidar DEM acquired in 2021 by Taranaki Regional Council available

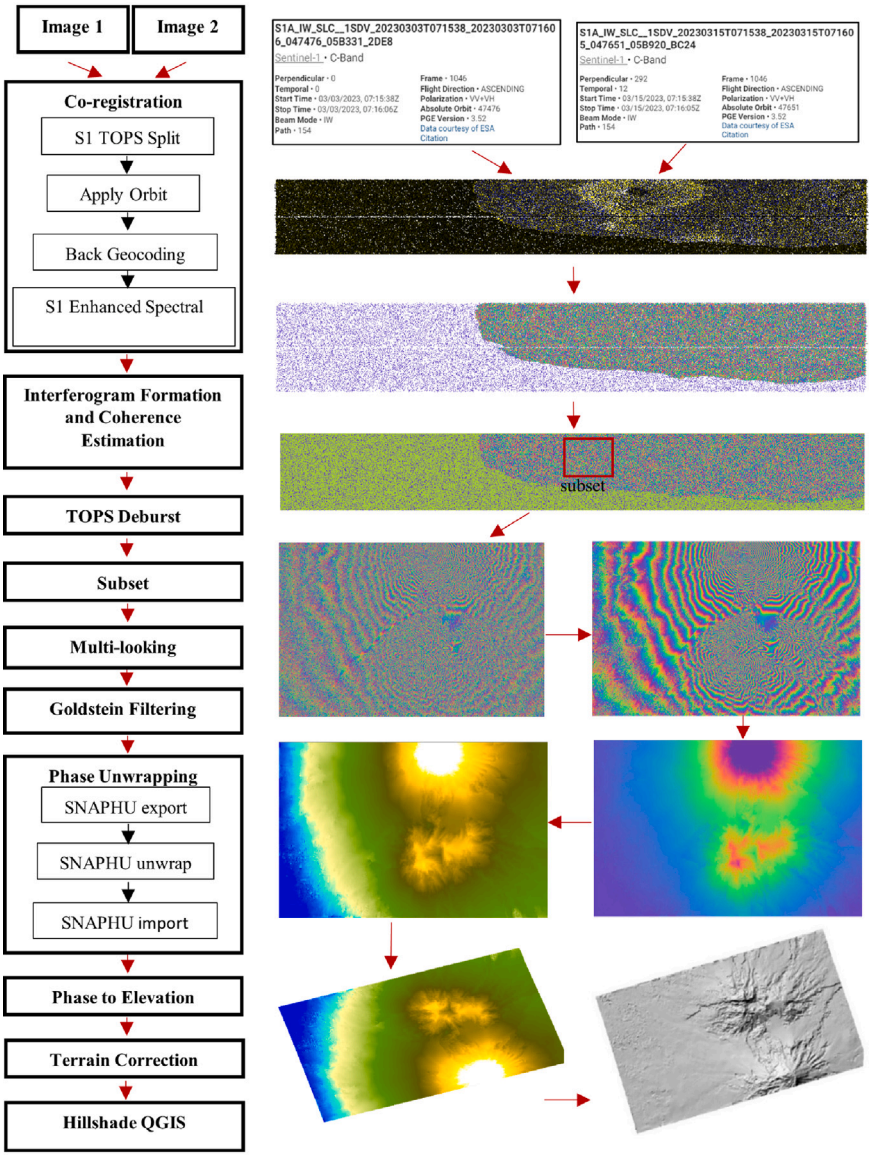

Fig. 2. Flow diagram summarizing the processing steps to generate a DEM using SNAP. Illustrations represent the results from the main steps following the red arrows. Phase unwrapping is done using the Statistical-Cost, Network-Flow Algorithm for Phase Unwrapping SNAP complement (Chen and Zebker, 2001).

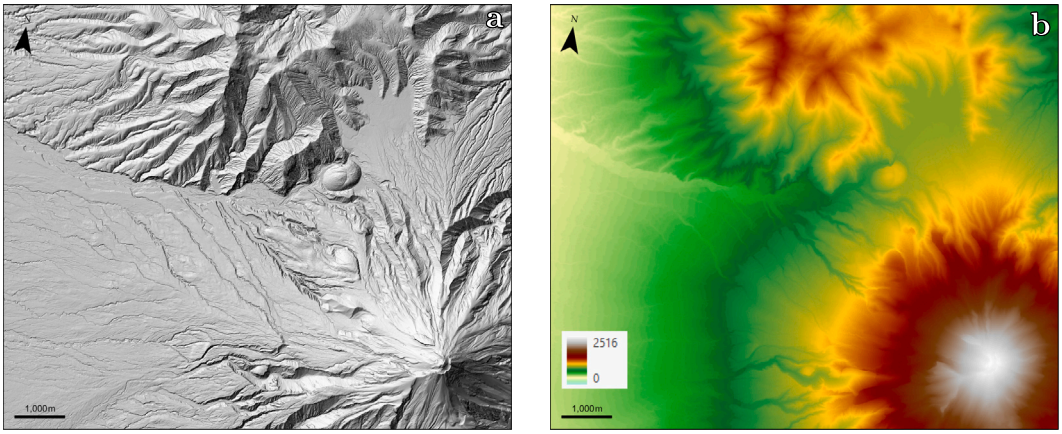

(a) (b)

Fig. 3. (a) Hillshade representation of Lidar DEM and (b) associated elevation in meters above sea level.

Table 1
Pairs of images used to generate DEMs and their nomenclature for the rest of the paper.

Orbit	Year	Characteristics				DEM created
		Image 1	Image 2	B_T (days)	$B_\perp$ (m)	
Ascending	2015	1 February	25 February	24	236	2015 February
		25 February	21 March	24	208	2015 March
	2017	14 February	4 March	18	150	2017 February
	2018	15 February	11 March	24	167	2018 February
		23 March	4 April	12	165	2018 March
	2021	6 January	30 January	24	187	2021 January
		11 February	7 March	24	222	2021 February
	2023	3 March	15 March	12	292	2023 March
Descending	2017	14 April	26 April	12	163	2017 April
	2021	17 April	29 April	12	161	2021 April
	2023	7 April	19 April	12	238	2023 April

Table 2
TPI landscape classification modified after Weiss (2001). Colour scale used for results representation.

Key	Class	Landscape	Unit (STDV)
	1	Valleys	< -1
	2	Lower slope	$-1 < x \leq -0.5$
	3	Concave middle/flat slope	$-0.5 < x \leq 0$
	4	Convex middle/flat slope	$0 < x \leq 0.5$
	5	Upper slope	$0.5 < x \leq 1$
	6	Ridge	> 1

Table 3
Proprieties of initial pile material modified after Procter et al. (2009a).

Parameter	Value
Pile Shape	Paraboloid
Pile Height	118.95 m
Location of Centre	245781, 5646589 (UTM 60S)
Radii	254.89 m; 181.25 m
Orientation	155°
Internal friction	30°
Bed friction	20°

on the LINZ website, as a reference, assuming that no major surface changes have occurred between 2015 and 2023 (Fig. 3). The spatial resolution of the Sentinel-1 generated DEMs is 11.5 × 14.8 m. We resample all DEMs to 15 × 15 m and adjust their spatial extent, as this change slightly according to the orbit used, allowing us to perform a pixel-by-pixel comparison. Root Mean Square Error (RMSE) is commonly used to express the vertical accuracy of a DEM with relation to another using the following equation:

$$\mathrm{RMSE} = \sqrt{\frac{1}{N}\sum_{n=1}^{N}(H_n - h_n)^2} \tag{2}$$

Where N represents the total number of pixels, n a specific pixel, H and h the elevation height of the specific pixel in the reference and generated DEM respectively (Borlaf-Mena et al., 2020).

3.2. Topographic position index (TPI)

Incising valleys act as a gully for sediment accumulation fed by the erosion of the upper slopes and ridges in the headwaters, while lower and mid/flat slopes transport the material into the depositional ring plain area. Stony-Hangatahua River is fed by several incising catchments all joining the main channel, which progressively fades into a gentle flat slope as it flows towards the NW. To evaluate how well the SAR DEM characterizes and identifies channels across Mount Taranaki, we use the Topographic position index (TPI) tool. This QGIS implemented tool assigns an elevation value to each cell calculated by averaging the values of the neighbouring pixels.

Ridges and hilltops will produce a positive value as the point is higher than surrounding pixels, while valleys will generate a negative TPI. Landscapes are classified using standard deviation units (STDV) as described in Weiss (2001) and in Table 2. For values close to zero (middle/flat slopes), we separate them according to their convex (positive) or concave (negative) shape. Using STDV to classify TPI values was described by Weiss (2001) as a more "sophisticated" method that takes into account the variability of elevation values within the neighbourhood. The level of accuracy in the landscape classification is dependent on the scale of the geographic area studied and the pixel search radius. A smaller radius will highlight the finer landscape details such as individual streams and ridge lines, while a larger radius will classify the major ridges and canyons. We select a neighbourhood of 800 m to identify the major structures while considering the global spatial geomorphology of the volcano. We compute the TPI on our best results from the ascending and descending orbit to compare to a LiDAR derived classification. To assess the accuracy of the classification, we compute the True Positive Rate (TPR) (Eq. (3)) for each landscape class (1–6) and the Overall Accuracy (OA) (Eq. (4)) which indicates the degree of agreement between the InSAR and LiDAR TPI's (with 1 being perfect agreement and 0 no agreement) using the following equations:

$$TPR = \frac{TP}{TP + FN} \tag{3}$$

$$\mathrm{OA} = \frac{\mathrm{TP}_1 + \mathrm{TP}_2 + \cdots + \mathrm{TP}_n}{N} \tag{4}$$

Where TP represents true positive, FN false negative and N the total number of pixels.

3.3. Mass flow simulations using Titan2D

Titan2D (Patra et al., 2005; Simakov et al., 2019; Patra et al., 2020) is a LINUX based code which uses a depth averaged approximation for an incompressible "shallow water", Coulomb granular flows (Charbonnier et al., 2015; Procter et al., 2009b). The thickness of the deposits is assumed to be small compared to the spatial extent of the inundated area allowing the simulation of a 3D flow across a natural terrain utilizing an adaptive mesh (Patra et al., 2005). Users control the simulations by indicating the dimensions of the initial pile of material which includes its height, shape, volume, location, and footprint but also defining its angle of internal friction and angle of basal friction. In this study, the terrain is the Sentinel-1 generated DEM, and outputs of the simulations provide a pile height, x-momentum and y-momentum for each point in the grid. The parameters used in our models (Table 3) are derived from the simulations of the most recent dome collapses on

Table 4
Hillshade representation for each generated DEM for the ascending orbit and its difference with relation to LiDAR DEM. Colour scales are identical and fixed between −500 m and 500 m to have a clearer and constant representation throughout each image. Scale and orientation are identical for each figure highlighted in the first row. Associated RMSE for each DEM compared to LiDAR.

Date	DEM Hillshade	LIDAR-DEM
2015 February	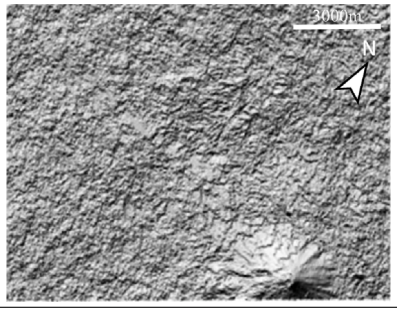	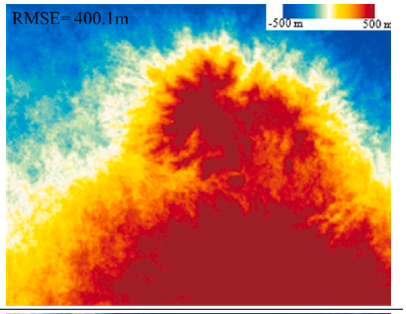
2015 March	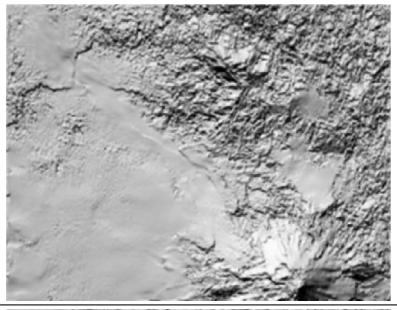	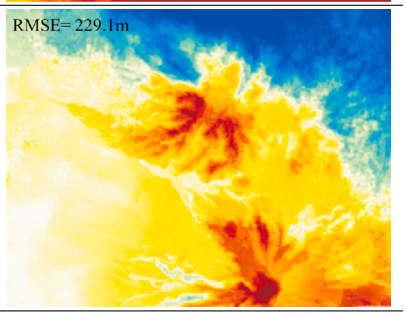
2017 February	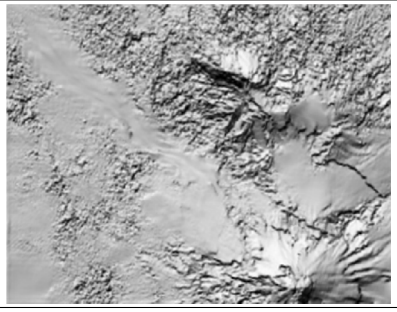	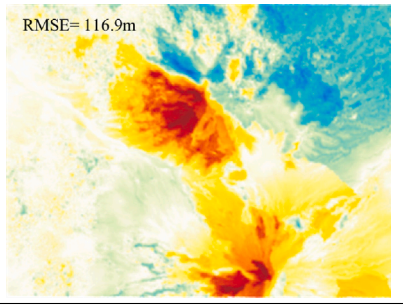
2018 February	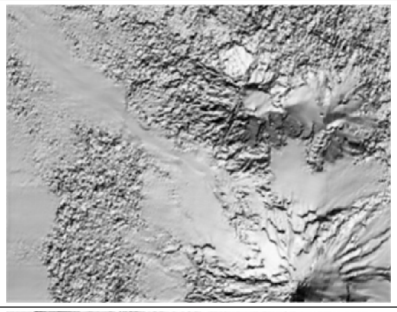	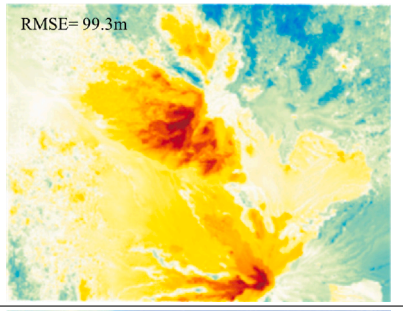
2018 March	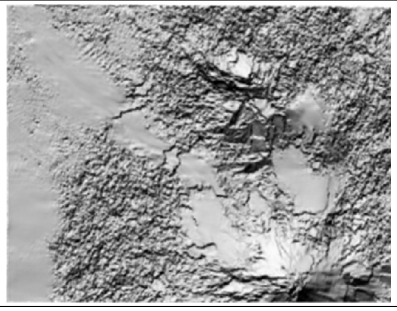	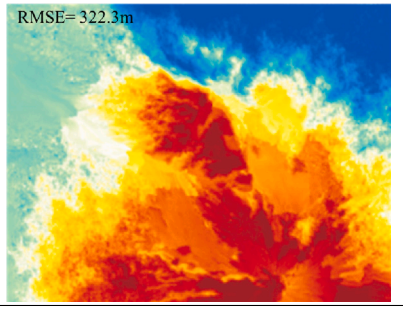

(*continued on next page*)

the northwestern side of Mount Taranaki carried out by Procter et al. (2009a). The initial volume, shape and position of the collapsing pile was estimated from current crater geomorphology. In our simulations, the coordinates of the centre of the pile were slightly modified due to geometric distortions occurring near the summit of the volcano. Basal/internal friction angles are derived from 80 simulations for which

Table 4 (*continued*).

Date	DEM Hillshade	LIDAR-DEM
2021 January	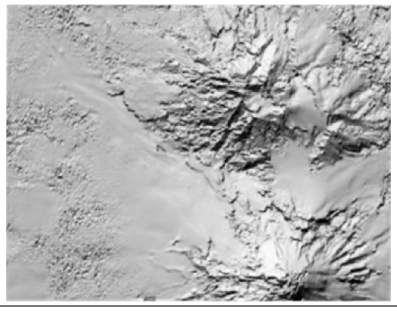	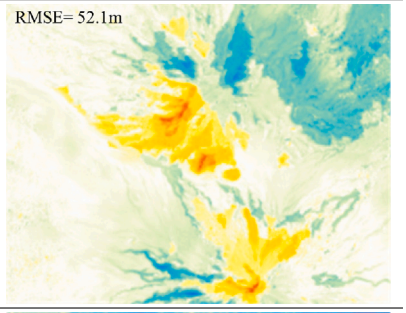
2021 February	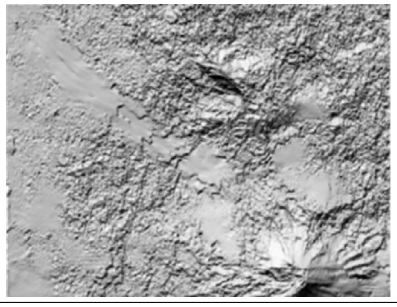	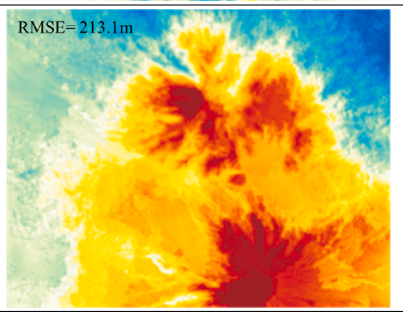
2023 March	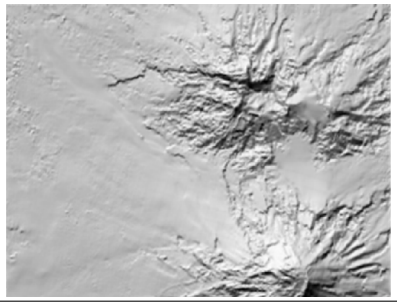	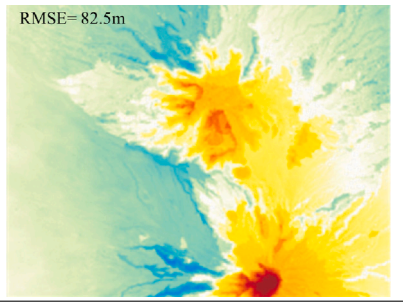

the angles vary at 5° intervals to compare inundated area, run-out distance, and volume outputs to true mapped deposits. Results from mass flow simulations are commonly combined for hazard analysis.

To evaluate the performance of our mass flow simulations in relation to the same simulations performed on the LiDAR DEM, we calculate positive predictive value (PPV)(Eq. (5)), TPR (Eq. (3)) and critical success index (CSI) (Eq. (6)) for both models defined by the following equations (Mead et al., 2021):

$$\mathrm{PPV} = \frac{TP}{TP + FP} \tag{5}$$

$$\mathrm{CSI} = \frac{TP}{TP + FP + FN} \tag{6}$$

Where FP false positive and TN true negative, obtained by pixel classification comparison of simulation results for LiDAR and InSAR. In the case of BAFs, we classify the results as inundated/non-inundated binary system, using a 1 m deposit thickness as threshold value. Areas inundated in both the LiDAR and InSAR simulations are classified as TP, while non-inundated areas are classified as TN. Inundated areas in the LiDAR model but not in the InSAR are classified as FN, and inversely, inundated areas in the InSAR model that are not in the LiDAR are classed as FP. PPV therefore represents the proportion of correctly simulated pixels within the InSAR footprint. Sensitivity highlights the proportion of pixels identified as inundated in the InSAR model within the inundated LiDAR footprint. Finally, CSI represents the proportion of correctly modelled areas within a combined InSAR and LiDAR inundated footprint (Mead et al., 2021).

4. Results

4.1. Accuracy assessment

Overall, the absolute accuracy of the InSAR DEMs generated from both orbits (Table 4 and Table 5) is poor from an absolute measure with elevation differences of several hundred meters being observed in some areas as compared to the LiDAR DEM. 2021 January and 2023 March DEMs are the most accurate with a RMSE of 52.1 m and 82.5 m, respectively Table 4. Due to its higher coherence, the general conical shape of Mount Taranaki is well defined despite its overall height being underestimated by the generated DEMs. Looking at the spatial distribution of the elevation errors in Table 4 and Table 5, the slopes facing towards the sensor and the slopes near the summit of the volcano facing away from the sensor in respective orbits have the strongest inaccuracy due to the side looking nature of SAR acquisitions. Slopes facing towards the sensor are sensitive to layover and foreshortening, while sections near the summit, facing away from the sensor generate little to no backscattering due to shadowing effects. The incidence angle of the emitted signal is lower than the steep local topography, meaning that certain areas are not illuminated inducing gaps in the data. These observations highlight the importance of using data acquired from a specific orbit according to the geomorphological setting of our area of study. The ruggedness of the hillshade observed across the ring plain and the slopes of Mount Pouakai in most DEMs result from lower coherence and noise within the signal which subsequently leads to faulty unwrapping. This generates a ramp across the image as clearly seen from the blue to red colour pattern in most figures, with values converging from negative in the ring plain to positive towards the summits. The elevation of shallower/flat slopes is generally overestimated

Table 5
Hillshade representation for each generated DEM for the descending orbit and its difference with relation to LiDAR DEM. Colour scales are identical and fixed between −500 m and 500 m to have a clearer and constant representation throughout each image. Scale and orientation are identical for each figure highlighted in the first row. Associated RMSE for each DEM compared to LiDAR.

Date	DEM Hillshade	LIDAR-DEM
2017 April	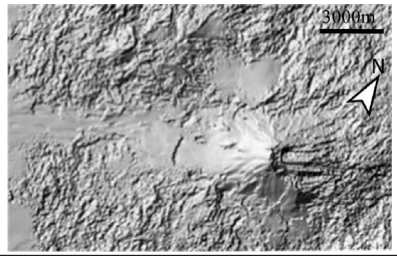	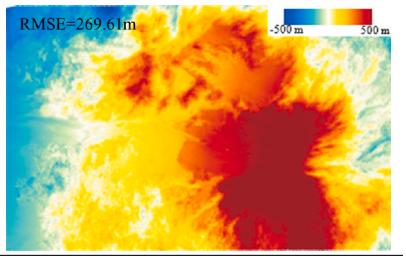
2021 April	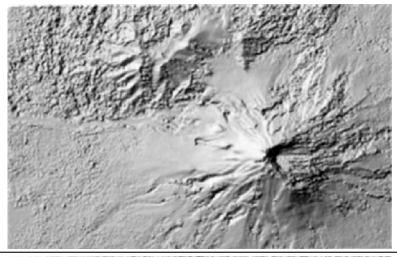	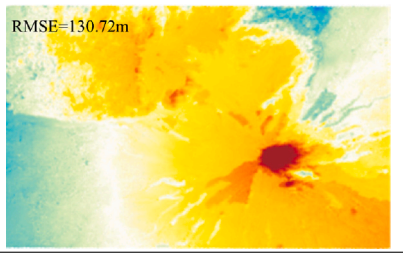
2023 April	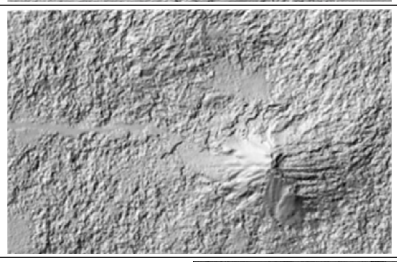	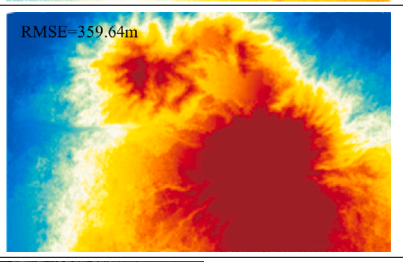
LIDAR	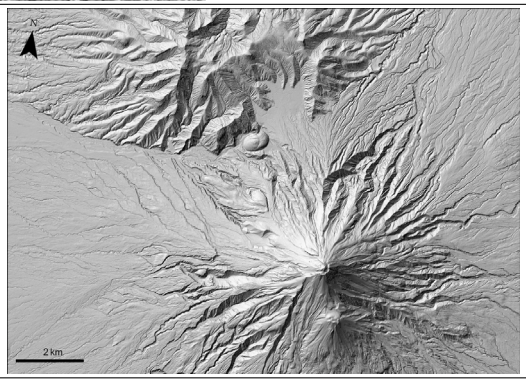	

while that of steeper slopes is underestimated. This spatial pattern was also observed in the paper of Braun (2021) and is a result of faulty unwrapping.

4.2. Channel identification

Absolute elevation values recorded by our generated DEMs are clearly inaccurate. In the context of mass flow simulations, the strongest control on runout distance and propagation path will result from channelization effects induced by ridges and valleys and slope angles. Using STDV units as TPI thresholds de-emphasizes class 2 and 5 resulting from a narrower value range lowering the number of pixels to compare as mentioned in Weiss (2001). A similar pattern is observed in terms of TPR across each class, with class 3 and 4 being the most accurately identified, followed by ridges (class 6) and valleys (class 1)(Fig. 4). Class 2 and 5 are very poorly classified due to lower pixel counts. The OA for each TPI is represented in lower values of the classification suggesting a relatively poor accuracy between our InSAR and LiDAR DEMs. The fair identification of ridges in January 2021 (0.578) and April 2021 (0.602) is a positive observation as these geomorphological features strongly control the channelization of gravitational flows such as lahars or debris avalanches.

4.3. BAFs simulation result

We use Titan2D to perform BAFs simulations using January 2021 (ascending), April 2021 (descending) and LiDAR DEMs as terrain models as these have the highest TPR values for ridges and valleys. Due to the geometric distortions previously discussed, the SE section of the crater is strongly overlooked and is represented as a "cliff" in the April 2021 descending DEM (seen in Table 5). This required the dome position/initial pile to be offset (new centre coordinates E245781, N5646589 UTM 60S) from the previous study (Procter et al., 2009a) to be able to generate BAFs down this non-realistic SE cliff section. The offset pile position was able to simulate the collapse of a dome down along the NW flank, to ensure a propagation of flow into the Stony River for both orbits (Fig. 5). The final deposit thickness distribution

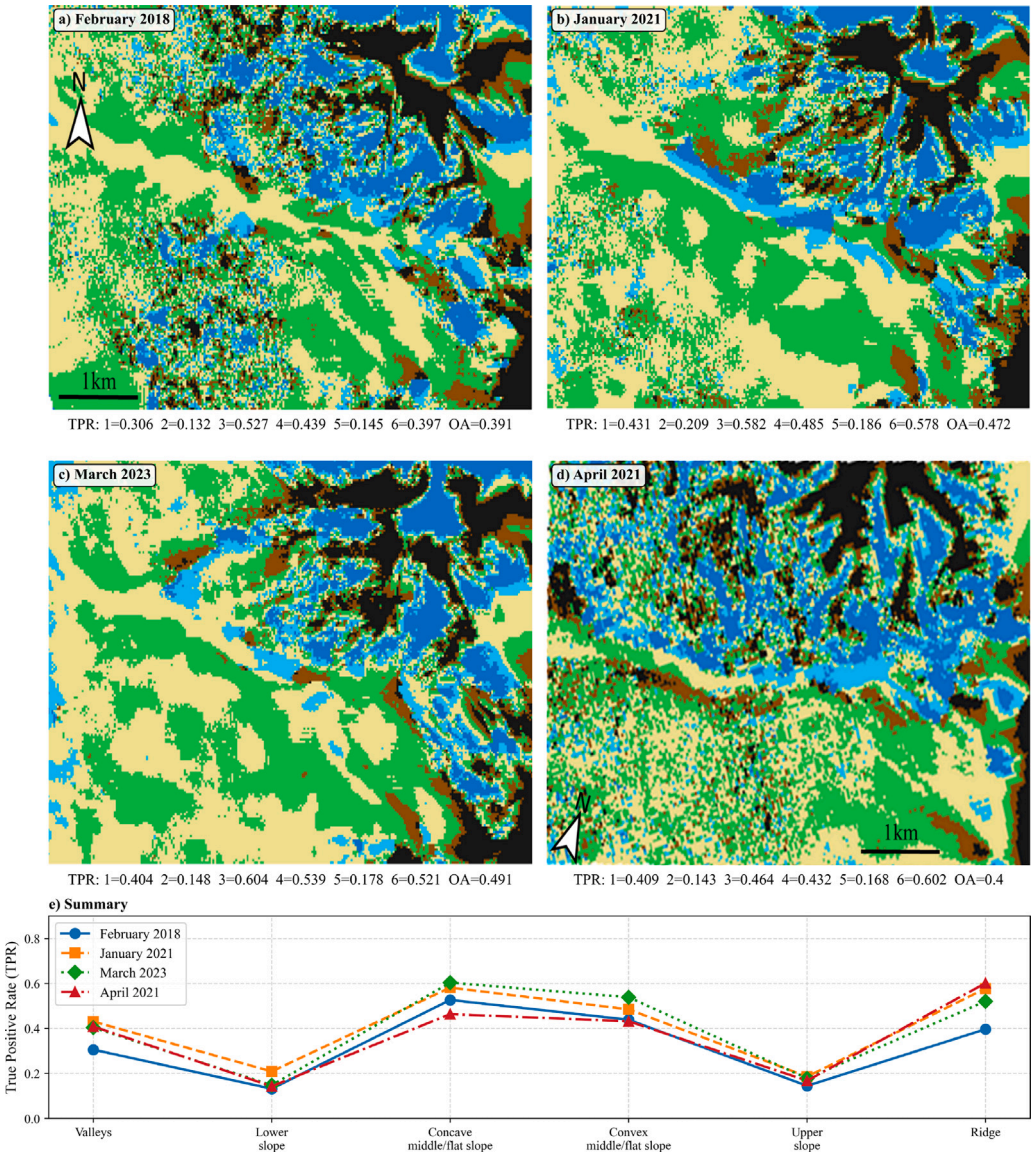

Fig. 4. TPI classification results and associated performance metrics for (a-c) ascending and (d) descending orbits and summarized in (e) Colour scale from Table 2 where 1= Valleys (blue), 2 = Lower slope (cyan), 3= Concave middle/flat slope (beige), 4= Convex middle/flat slope (green), 5= Upper slope (Brown) and 6= Ridge (black). Beneath each panel are reported the True Positive Rates (TPR) for each landscape class (1–6) and the Overall Accuracy (OA) of the classification.

can be visualized in QGIS, using 1 m as an inundated threshold value to determine flow extent.

The lateral extent of inundated footprint for each simulation is comparable with a maximum width of 4 km perpendicular to the main NW flow direction (Fig. 5). The run-out extent, however, is less important in our InSAR simulations with a maximum distance of 3 km compared to the 4.7 km in the LiDAR. The Heim coefficient (H/L) is commonly used to identify run-out distance of a mass flow with relation to the local topography (Procter et al., 2009a). This is obtained by dividing the total height drop between the DEM source and the furthest deposition point, with the horizontal distance between these two points (Chang et al., 2021). We obtain values of 0.292 for both InSAR simulations, and 0.261 for LiDAR. This occurs from our InSAR DEMs having a lower slope angle due to the elevation under-estimation of the volcanic flanks. The valley catchments observed in the LiDAR DEM behave as a gully, channelizing the BAFs and concentrating the momentum propagating further down slope until reaching the Stony River valley (Fig. 5). The InSAR inundation footprints have a simpler, fan shape deposit due to the volcano slopes being shallower and less channelized, with BAFs rapidly losing momentum. The increase in topography roughness observed in the InSAR DEMs due to noise within the SAR images also leads to higher simulated momentum loss and therefore shorter travel distance. The performance metrics of both InSAR DEM based simulations with relation to the LiDAR based simulations used as a reference are represented in Fig. 6 for a simulation thickness of up to 20 m. The positive predictive value (PPV) increases with thickness deposit (Fig. 6.a and Fig. 6.b) with a more rapid rate for the April derived DEM simulations (Fig. 6.a), indicating that this InSAR DEM is less

likely to be inaccurate for the thicker components of the simulation outputs. This simulation produces accurate predictions over broader thicknesses. PPV in the January derived DEM based simulations (Fig. 6.b) gradually increase indicating low confidence predictions. TPR behaves inversely to PPV but follows a similar pattern with values rapidly dropping for increasing thicknesses for the April 2021 DEM derived (Fig. 6.e), while the drop is more progressive in response to the January 2021 data (Fig. 6.f). CSI values above 0.5 indicate the range of simulation thicknesses which there are more correctly identified comparisons than incorrect comparisons (Mead et al., 2021). This value is obtained for thickness values below 1.04 m in January 2021 (Fig.

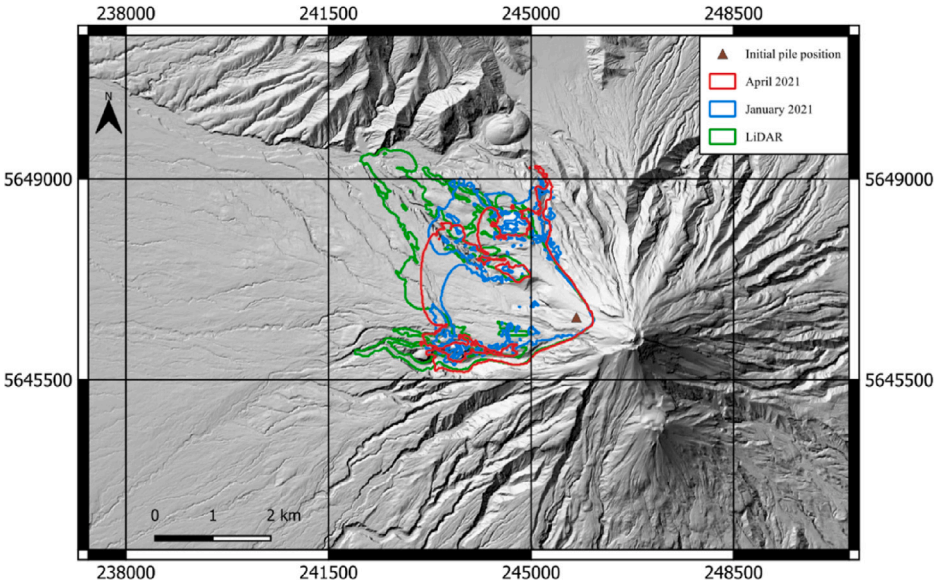

Fig. 5. Spatial extent of inundated areas for each simulation for a 1 m thickness threshold. Base image is LiDAR DEM.

6.d) and 2.39 m for April 2021 (Fig. 6.c), demonstrating that our simulations perform better for a very narrow range of thicknesses. These results show that the simulations based on April 2021 DEM produced less inaccurate results, however overall, all InSAR generated DEM based simulations showed very little agreement to the LiDAR based simulations.

5. Discussion

5.1. Sentinel-1 DEM generation for steep and vegetated volcanic terrains

The strong elevation differences obtained from our InSAR generated DEMs has shown the strong limitations to applying Sentinel-1 SAR data for rapid DEM generation in steep and wet environments such as Mount Taranaki. The absolute accuracy of the DEMs (in comparison to the LiDAR DEM) generated topographic anomalies due to temporal decorrelation, resulting from volumetric scattering induced by changes in humidity, pressure, temperature, wind and structure of ground features in the surrounding dense tropical vegetation (White et al., 2015). Several methods have been proposed in the literature to correct elevation-dependent (Dogru et al., 2023; Remy et al., 2003) and long-wavelength atmospheric artifacts (e.g., Doin et al., 2009; Li et al., 2006) for ground deformation monitoring, but little has been proposed for DEM generation. Methods to increase DEM quality by reducing the impact of temporal decorrelation such as stacking and averaging results (Ibarra et al., 2024) obtained from different interferograms, or masking low coherence areas (Braun, 2021) during the SNAP processing, were tested but showed no better results and therefore ignored in this study. Stronger coherence between the SAR images is required to generate accurate DEMs. Using longer wavelengths (L-band) may also reduce the impact of the forest canopy (Pinel et al., 2011) as the signal would penetrate through it, however this would reduce the ground resolution of the DEM. L-band satellites also tend to have longer temporal resolutions limiting the number of acquisitions.

Geometric distortions also impact the most important sections of the volcano such as the summit crater and its upper flanks. New dome formation and collapses are most likely to occur in the same summit area based on the volcano's most recent eruptive history (Lerner et al., 2019; Platz et al., 2012; Procter et al., 2009a). This suggests that geomorphological changes occurring near the summit crater may not be able to be identified in future InSAR DEM's. This would also require waiting for acquisitions from the correct orbit. Combining ascending and descending data to produce a single DEM did not help reduce the geometric distortions near the summit. Furthermore, perpendicular baselines between acquisitions are not always suitable for DEM generation which restrains the data available to use in the case of an event. Altogether, there are too many uncertainties and conditions required to integrate Sentinel-1 into generating accurate DEMs for steep, vegetated areas such as Mount Taranaki. These observations and conclusions are consistent with the current state of research observed in the literature (e.g., Mohammadi et al., 2020; Braun, 2021; Chindo et al., 2023). However, DEM generation from Sentinel-1 may be suitable for other low lying, non-vegetated volcanoes on the ring-plain and in particular those portions of the Stony-Hangatahua River that are 5–10 km from source. These areas for Mt. Taranaki are also where the impacts from mass flows are most hazardous suggesting that despite the inaccuracies identifying flow paths and channels does provide some useful information for a rapid hazard analysis.

5.2. Flow hazard modelling at stratovolcanoes using Sentinel-1 generated DEMs

We have shown that despite being of low accuracy in terms of absolute elevation, InSAR offers the possibility to produce an up-to-date DEM of Mount Taranaki within a 12-day revisit interval, which can be integrated for BAFs modelling/simulation and hazard assessment. Although this study was conducted using a 12-day repeat cycle, the temporal resolution has been restored to 6 days since April 2025 following the launch of Sentinel-1C, effectively reducing the repeat cycle and providing a cost-free, repeatable methodology particularly valuable for remote or under-monitored volcanoes. Hazard maps indicate the probability of a specific hazard likely to occur within a given set of uncertainties defined by the input parameters (Dalbey et al., 2008). Typical flow modelling measures involved in hazard map creation are mean thickness distribution, used to estimate the areas at risk for burial of human or buildings, and in some cases flow speed for tree or building blow down (Dalbey et al., 2008). In our situation, initial parameters are defined from past BAFs deposits analysis and numerical modelling (Procter et al., 2009a) representing a single dome collapse event. However, typical hazard assessment should take into consideration the variety of possible outputs for a given set of realistic input possibilities (e.g., volume, internal and bed friction). Our simulations showed that the BAFs have a similar lateral inundation extent in the upper section of the volcano due to its relatively simple conic shape and

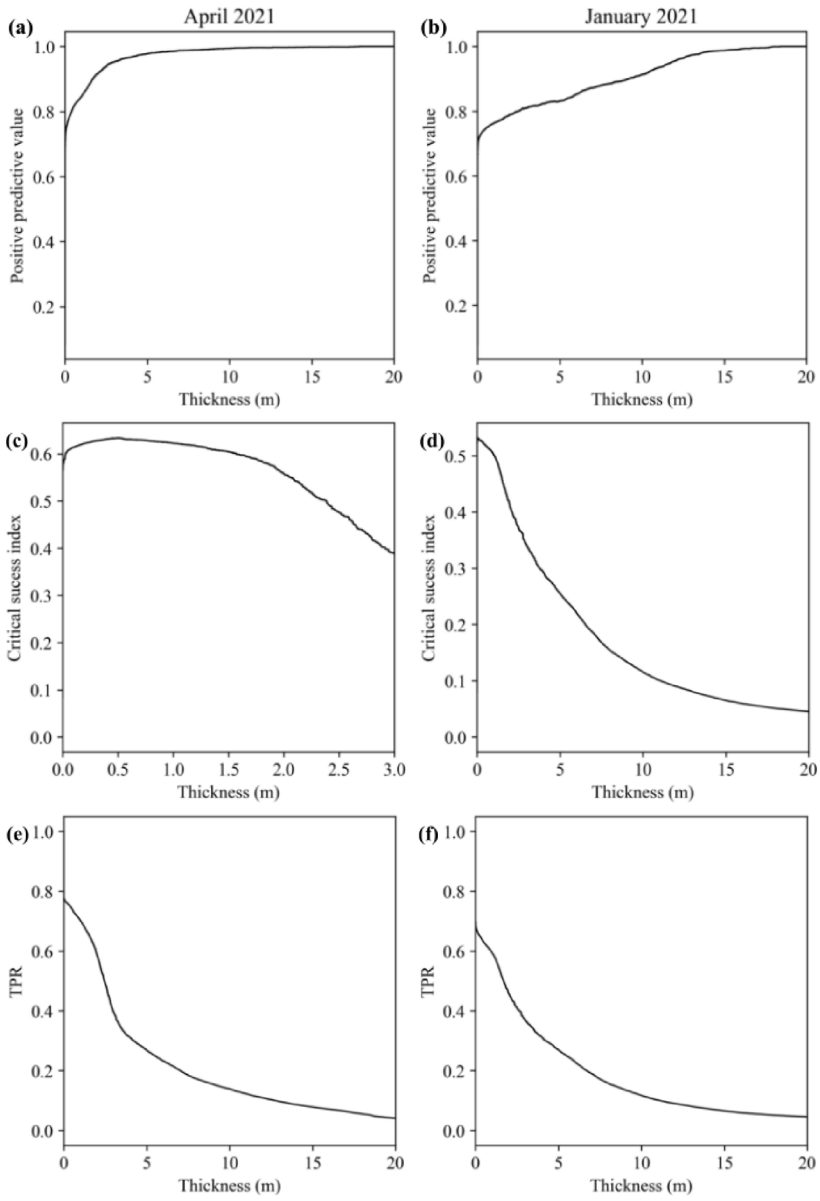

Fig. 6. Performance analysis of BAFs simulations showing (a) PPV, (b) CSI and (c) TPR according to the thickness of the BAFs deposits.

where valleys are broader and deeper. The major differences occur at its base over shallower slopes, where channel incision is more complex. These channels are more sinuous, less deep and narrower behaving as a funnel, concentrating the flows energy, allowing BAFs to propagate further. Similar observations were made in Stevens et al. (2003), where lahar modelling at Mount Ruapehu agreed on the upper section where slope angle > 4°. Differences occur in the lower section due to complexity of the channels and the forest cover. These simulations were carried out on DEMs derived from topographic contour lines and from airborne C-band NASA AIRSAR system. This suggests that for similar stratovolcanoes, the elevation inaccuracies resulting from the InSAR processing, are less impacting in terms of hazard assessment than the lack of channel identification defined by slope features and curvature. It goes without saying that elevation values still need to be within a logical range and agree with the general geomorphology of the volcano allowing gravity driven flows to propagate. Positively identifying ridges and valleys as highlighted by our TPI classification may be more important for rapid mass flow hazard assessment. If absolute elevation values are shifted globally across the area due to low quality unwrapping but preserve the overall shape and structure, InSAR generated DEMs may still be useful for BAFs modelling as they give a first insight on potentially impacted areas. The study of Huggel et al. (2008) showed that despite being of higher resolution, the 30 m ASTER generated DEM at Popocatépetl was less reliable than the 90 m resolution SRTM DEM for lahar modelling due to its inaptitude to identify deep incising valleys, impacting the predicted flow path. Similar observations are made in the study of Mohammadi et al. (2020) where Sentinel-1 generated DEMs failed to accurately identify hydrological networks in vegetated areas, compared to other open-access, lower resolution DEMs. Stefanescu et al. (2012) also highlighted that simulations using finer resolution DEMs are more costly and should be considered for lower flow volumes ($>10^5$ m^3), which will be more sensitive to minor topographic changes, impacting the inundation path. Historically, BAFs on the NW side of Mount Taranaki have been estimated to be a minimum volume of 5×10^6 m^3 (Procter et al., 2009a), and our simulations were computed for a typical volume of 1×10^6 m^3 suggesting that our modelling does not require high resolution DEMs. Large volumes of flow will be less affected by minor topographic changes which may not be detected in the Sentinel-1 InSAR DEMs.

6. Conclusion

Radar remote sensing data is a powerful tool for monitoring and analysing volcanic activity and the associated hazards such as debris flows, lahars, and mass flows. This study assessed the suitability of Sentinel-1 for generating DEMs of Mt. Taranaki in New Zealand for mass flow simulations to determine potential hazard impact. Results of the simulations show that the run-out extent of the inundated area and the thickness of the deposits strongly vary due to the quality of the DEM used for the simulations, especially on the accuracy of channel identification. The lack of coherence between our SAR images and geometrical distortions due to the steepness of the volcano, and the dense vegetation cover lead to inaccurate DEMs significantly impacting our final hazard assessment. All together there are too many conditions required to accurately integrate Sentinel-1 generated DEMs into rapid mass flow hazard assessment for steep vegetated stratovolcanoes. However, Sentinel-1 SAR products remain critical for numerous hazard studies credit to its open access and short global surveying policies allowing continuous monitoring and adapted decision making. Recently launched commercial radar satellites such as ICEYE constellation offer exciting new surveying prospects with near real-time Earth observations which would limit temporal decorrelation and therefore increase the quality of our data. However, efforts are still to be made to enable data accessibility for scientific communities. Plans for new L-band SAR satellites missions with shorter temporal resolution such as Tandem-L, ALOS-4 and NISAR (Aoki et al., 2021) will also allow more frequent acquisitions which may be more suitable for DEM generation in environments such as Mount Taranaki.

CRediT authorship contribution statement

Samuel McGowan: Writing – original draft, Visualization, Methodology, Investigation, Formal analysis, Data curation, Conceptualization. **Jonathan Procter:** Writing – review & editing, Supervision, Resources, Methodology, Investigation, Funding acquisition, Conceptualization. **Stuart Mead:** Writing – review & editing, Supervision, Methodology, Conceptualization. **Gabor Kereszturi:** Writing – review & editing, Supervision, Methodology.

Declaration of competing interest

The authors declare that they have no known competing financial interests or personal relationships that could have appeared to influence the work reported in this paper.

Acknowledgment

This project is funded by the 'Transitioning Taranaki to a Volcanic Future' Research Programme of the Ministry of Business, Innovation and Employment's Endeavour Fund.

Data availability

Data will be made available on request.

References

Albino, F., Biggs, J., 2021. Magmatic Processes in the East African Rift System: Insights From a 2015–2020 Sentinel-1 InSAR Survey. Geochem. Geophys. Geosystems 22 (3), http://dx.doi.org/10.1029/2020GC009488.

Albino, F., Biggs, J., Escobar-Wolf, R., Naismith, A., Watson, M., Phillips, J.C., Marroquin, G.C., 2020. Using TanDEM-x to measure pyroclastic flow source location, thickness and volume: Application to the 3rd June 2018 eruption of Fuego volcano, Guatemala. J. Volcanol. Geotherm. Res. 406, 107063, Publisher: Elsevier.

Albino, F., Smets, B., d'Oreye, N., Kervyn, F., 2015. High-resolution TanDEM-x DEM: An accurate method to estimate lava flow volumes at Nyamulagira Volcano (d. r. Congo). J. Geophys. Res.: Solid Earth 120 (6), 4189–4207. http://dx.doi.org/10.1002/2015JB011988.

Andaru, R., Rau, J.-Y., Prayoga, A.S., 2022. Determination of potential secondary lahar hazard areas based on pre-and post-eruption UAV DEMs: Automatic identification of initial lahar starting points and supplied lahar volume. Int. J. Appl. Earth Obs. Geoinf. 115, 103096, Publisher: Elsevier.

Aoki, Y., Furuya, M., De Zan, F., Doin, M.-P., Eineder, M., Ohki, M., Wright, T.J., 2021. L-band Synthetic Aperture Radar: Current and future applications to Earth sciences. Earth, Planets Space 73 (1), 56. http://dx.doi.org/10.1186/s40623-021-01363-x.

Bamler, R., Hartl, P., 1998. Synthetic aperture radar interferometry. Inverse Problems 14 (4), R1.

Bemelmans, M.J., Biggs, J., Poland, M., Wookey, J., Ebmeier, S., Diefenbach, A.K., Syahbana, D., 2023. High-resolution InSAR reveals localized pre-eruptive deformation inside the crater of Agung Volcano, Indonesia. J. Geophys. Res.: Solid Earth 128 (5), http://dx.doi.org/10.1029/2022JB025669.

Betts, H., Neall, V., Procter, J., 2010. Erosion monitoring in the upper Stony River catchment, Egmont National Park, Taranaki.. Technical Report LC0037, Landcare Research Ltd.

Borges, D.E., Ramage, S., Green, D., Justice, C., Nakalembe, C., Whitcraft, A., Barker, B., Becker-Reshef, I., Balagizi, C., Salvi, S., 2023. Earth observations into action: the systemic integration of earth observation applications into national risk reduction decision structures. Disaster Prev. Manag.: An Int. J. 32 (1), 163–185.

Borlaf-Mena, I., Santoro, M., Villard, L., Badea, O., Tanase, M.A., 2020. Investigating the Impact of Digital Elevation Models on Sentinel-1 Backscatter and Coherence Observations. Remote. Sens. 12 (18), http://dx.doi.org/10.3390/rs12183016.

Braun, A., 2021. Retrieval of digital elevation models from Sentinel-1 radar data – open applications, techniques, and limitations. Open Geosci. 13 (1), 532–569. http://dx.doi.org/10.1515/geo-2020-0246.

Chang, H., Ryou, K., Lee, H., 2021. Debris flow characteristics in flume experiments considering berm installation. Appl. Sci. 11 (5), 2336, Publisher: MDPI.

Charbonnier, S.J., Palma, J.L., Ogburn, S., 2015. Application of" shallow-water" numerical models for hazard assessment of volcanic flows: the case of titan2d and Turrialba volcano (Costa Rica). Rev. Geológica de América Central (52), 107–128.

Chaussard, E., Johnson, C.W., Fattahi, H., Bürgmann, R., 2016. Potential and limits of InSAR to characterize interseismic deformation independently of GPS data: Application to the southern San Andreas Fault system. Geochem. Geophys. Geosystems 17 (3), 1214–1229. http://dx.doi.org/10.1002/2015GC006246.

Chen, Z., Li, Y., Li, C., Liu, Y., Dong, X., Hu, C., 2022. Analysis of General Geometric Decorrelation in Interferometric SAR. IEEE Geosci. Remote. Sens. Lett. 19, 1–5. http://dx.doi.org/10.1109/LGRS.2022.3187070.

Chen, C.W., Zebker, H.A., 2001. Two-dimensional phase unwrapping with use of statistical models for cost functions in nonlinear optimization. J. Opt. Soc. Amer. A 18 (2), 338–351, Publisher: Optical Society of America.

Chen, Y., Zhang, G., Ding, X., Li, Z., 2000. Monitoring earth surface deformations with InSAR technology: principles and some critical issues. J. Geospatial Eng. 2 (1), 3–22.

Chien, S., Tanpipat, V., 2012. Remote sensing of natural disasters. In: Encyclopedia of Sustainability Science and Technology. Springer, pp. 8939–8952.

Chindo, M.M., Hashim, M., Rasib, A.W., 2023. Challenges of insar dem derivation with sentinel-1 sar in densely vegetated humid tropical environment. Int. Arch. Photogramm. Remote. Sens. Spat. Inf. Sci. XLVIII-4/W6-2022, 93–98. http://dx.doi.org/10.5194/isprs-archives-XLVIII-4-W6-2022-93-2023.

Choi, H., Jeong, J., 2019. Speckle Noise Reduction Technique for SAR Images Using Statistical Characteristics of Speckle Noise and Discrete Wavelet Transform. Remote. Sens. 11 (10), http://dx.doi.org/10.3390/rs11101184.

Crosetto, M., Monserrat, O., Cuevas-González, M., Devanthéry, N., Crippa, B., 2016. Persistent Scatterer Interferometry: A review. ISPRS J. Photogramm. Remote Sens. 115, 78–89. http://dx.doi.org/10.1016/j.isprsjprs.2015.10.011.

Dalbey, K., Patra, A.K., Pitman, E.B., Bursik, M.I., Sheridan, M.F., 2008. Input uncertainty propagation methods and hazard mapping of geophysical mass flows. J. Geophys. Res.: Solid Earth 113 (B5), http://dx.doi.org/10.1029/2006JB004471.

Davila, N., Capra, L., Gavilanes-Ruiz, J., Varley, N., Norini, G., Vazquez, A.G., 2007. Recent lahars at Volcán de Colima (Mexico): drainage variation and spectral classification. J. Volcanol. Geotherm. Res. 165 (3–4), 127–141.

Deng, F., Rodgers, M., Xie, S., Dixon, T.H., Charbonnier, S., Gallant, E.A., López Vélez, C.M., Ordoñez, M., Malservisi, R., Voss, N.K., Richardson, J.A., 2019. High-resolution DEM generation from spaceborne and terrestrial remote sensing data for improved volcano hazard assessment — A case study at Nevado del Ruiz, Colombia. Remote Sens. Environ. 233, 111348. http://dx.doi.org/10.1016/j.rse.2019.111348.

Dogru, F., Albino, F., Biggs, J., 2023. Weather model based atmospheric corrections of Sentinel-1 InSAR deformation data at Turkish volcanoes. Geophys. J. Int. 234 (1), 280–296. http://dx.doi.org/10.1093/gji/ggad070.

Doin, M.-P., Lasserre, C., Peltzer, G., Cavalié, O., Doubre, C., 2009. Corrections of stratified tropospheric delays in SAR interferometry: Validation with global atmospheric models. Adv. SAR Interf. from 2007 Fringe Work. 69 (1), 35–50. http://dx.doi.org/10.1016/j.jappgeo.2009.03.010.

Dualeh, E.W., Ebmeier, S.K., Wright, T.J., Albino, F., Naismith, A., Biggs, J., Ordoñez, P.A., Boogher, R.M., Roca, A., 2021. Analyzing Explosive Volcanic Deposits From Satellite-Based Radar Backscatter, Volcán de Fuego, 2018. J. Geophys. Res.: Solid Earth 126 (9), http://dx.doi.org/10.1029/2021JB022250.

Dzurisin, D., 2006. Volcano Deformation: New Geodetic Monitoring Techniques. In: Springer Praxis Books, Springer Berlin Heidelberg.

Ezquerro, P., Bru, G., Galindo, I., Monserrat, O., García-Davalillo, J., Sánchez, N., Montoya, I., Palamà, R., Mateos, R., Pérez-López, R., González-Alonso, E., Grandin, R., Guardiola-Albert, C., López-Vinielles, J., Fernández-Merodo, J., Herrera, G., Béjar-Pizarro, M., 2023. Analysis of SAR-derived products to support emergency management during volcanic crisis: La Palma case study. Remote Sens. Environ. 295, 113668. http://dx.doi.org/10.1016/j.rse.2023.113668.

Farr, T.G., Rosen, P.A., Caro, E., Crippen, R., Duren, R., Hensley, S., Kobrick, M., Paller, M., Rodriguez, E., Roth, L., Seal, D., Shaffer, S., Shimada, J., Umland, J., Werner, M., Oskin, M., Burbank, D., Alsdorf, D., 2007. The Shuttle Radar Topography Mission. Rev. Geophys. 45 (2), http://dx.doi.org/10.1029/2005RG000183.

Ferretti, A., Monti-Guarnieri, A., Prati, C., Rocca, F., Massonet, D., 2007. InSAR Principles - Guidelines for SAR Interferometry Processing and Interpretation. ESA Train. Man. 19.

Gao, J., 2023. Remote Sensing of Natural Hazards, first ed. CRC Press, 10.1201/9781003354321.

Harvey, M., 2021. Sentinel-1 InSAR captures 2019 catastrophic White Island eruption. J. Volcanol. Geotherm. Res. 411, 107124. http://dx.doi.org/10.1016/j.jvolgeores.2020.107124.

Hay, S., 2000. An Overview of Remote Sensing and Geodesy for Epidemiology and Public Health Application. Adv. Parasitol. 47, 1–35. http://dx.doi.org/10.1016/S0065-308X(00)47005-3.

Hogenson, K., Kristenson, H., Kennedy, J., Johnston, A., Rine, J., Logan, T., Zhu, J., Williams, F., Herrmann, J., Smale, J., Meyer, F., 2020. Hybrid Pluggable Processing Pipeline (HyP3): A cloud-native infrastructure for generic processing of SAR data. http://dx.doi.org/10.5281/zenodo.4646138.

Holzer, T., Savage, J., 2013. Global earthquake fatalities and population. Earthq. Spectra 29 (1), 155–175. http://dx.doi.org/10.1193/1.4000106.

Hubbard, B., Sheridan, M., Carrasco-Núñez, G., Díaz-Castellón, R., Rodríguez, S., 2007. Comparative lahar hazard mapping at Volcan Citlalt??petl, Mexico using SRTM, ASTER and DTED-1 digital topographic data. J. Volcanol. Geotherm. Res. 160, 99–124. http://dx.doi.org/10.1016/j.jvolgeores.2006.09.005.

Huggel, C., Schneider, D., Miranda, P.J., Delgado Granados, H., Kääb, A., 2008. Evaluation of ASTER and SRTM DEM data for lahar modeling: A case study on lahars from Popocatépetl Volcano, Mexico. 1994-Present Erupt. Popocatépetl: Backgr. Curr. Act. Impacts 170 (1), 99–110. http://dx.doi.org/10.1016/j.jvolgeores.2007.09.005.

Ibarra, F., Cuello, A., Gotusso, L., Guerrieri, M., Ludueña, S., Marquez, J., Micou, A.P., Migliorini, R., Ortone, A., Perez, M., Posadas, A., Seco, J.L., Soldano, Á., Sotelo, A., Tamayo, C., Chiarito, E., 2024. Exploring c and l band InSAR digital elevation model stacking: A case study in Córdoba, Argentina. J. South Am. Earth Sci. 143, 105006. http://dx.doi.org/10.1016/j.jsames.2024.105006.

Journeau, C., Hreinsdottir, S., Hamling, I., 2021. Crustal deformation using GPS and InSAR analysis at Taupo volcano, New Zealand. http://dx.doi.org/10.1002/essoar.10507754.1.

Joyce, K., Samsonov, S., Manville, V., Jongens, R., Graettinger, A., Cronin, S., 2009. Remote sensing data types and techniques for lahar path detection: A case study at Mt Ruapehu, New Zealand. Remote Sens. Environ. 113, 1778–1786. http://dx.doi.org/10.1016/j.rse.2009.04.001.

Ketelaar, V., 2009. Satellite Radar Interferometry: Subsidence Monitoring Techniques. In: Remote Sensing and Digital Image Processing, Springer Netherlands.

Kubanek, J., Westerhaus, M., Schenk, A., Aisyah, N., Brotopuspito, K.S., Heck, B., 2015. Volumetric change quantification of the 2010 Merapi eruption using TanDEM-x InSAR. Remote Sens. Environ. 164, 16–25. http://dx.doi.org/10.1016/j.rse.2015.02.027.

Lerner, G.A., Cronin, S.J., Bebbington, M.S., Platz, T., 2019. The characteristics of a multi-episode volcanic regime: the post-AD 960 Maero Eruptive Period of Mt. Taranaki (New Zealand). Bull. Volcanol. 81 (11), 61. http://dx.doi.org/10.1007/s00445-019-1327-4.

Li, Z., Muller, J.-P., Cross, P., Albert, P., Fischer, J., Bennartz, R., 2006. Assessment of the potential of MERIS near-infrared water vapour products to correct ASAR interferometric measurements. Int. J. Remote Sens. 27 (2), 349–365. http://dx.doi.org/10.1080/01431160500307342, Publisher: Taylor & Francis.

Liu, X., 2008. Airborne LiDAR for DEM generation: some critical issues. Prog. Phys. Geogr. 32 (1), 31–49.

Manville, V., Major, J.J., Fagents, S.A., 2013. Modeling lahar behavior and hazards. Model. Volcan. Process.: Phys. Math. Volcanism 300–330, Publisher: Cambridge University Press Cambridge, UK.

Mead, S.R., Magill, C.R., 2017. Probabilistic hazard modelling of rain-triggered lahars. J. Appl. Volcanol. 6 (1), 8.

Mead, S., Magill, C., Hilton, J., 2016. Rain-triggered lahar susceptibility using a shallow landslide and surface erosion model. Geomorphology 273, 168–177. http://dx.doi.org/10.1016/j.geomorph.2016.08.022.

Mead, S.R., Procter, J., Kereszturi, G., 2021. Quantifying location error to define uncertainty in volcanic mass flow hazard simulations. Nat. Hazards Earth Syst. Sci. 21 (8), 2447–2460. http://dx.doi.org/10.5194/nhess-21-2447-2021.

Mohammadi, A., Karimzadeh, S., Jalal, S., Valizadeh Kamran, K., Shahabi, H., Homayouni, S., Al-Ansari, N., 2020. A Multi-Sensor Comparative Analysis on the Suitability of Generated DEM from Sentinel-1 SAR Interferometry Using Statistical and Hydrological Models. Sensors 20, 7214. http://dx.doi.org/10.3390/s20247214.

Muñoz-Salinas, E., Castillo-Rodríguez, M., Manea, V., Manea, M., Palacios, D., 2009. Lahar flow simulations using LAHARZ program: Application for the Popocatépetl volcano, Mexico. J. Volcanol. Geotherm. Res. 182 (1–2), 13–22.

Pallister, J.S., Schneider, D.J., Griswold, J.P., Keeler, R.H., Burton, W.C., Noyles, C., Newhall, C.G., Ratdomopurbo, A., 2013. Merapi 2010 eruption—Chronology and extrusion rates monitored with satellite radar and used in eruption forecasting. Merapi Erupt. 261, 144–152. http://dx.doi.org/10.1016/j.jvolgeores.2012.07.012.

Patra, A.K., Bauer, A.C., Nichita, C., Pitman, E.B., Sheridan, M.F., Bursik, M., Rupp, B., Webber, A., Stinton, A., Namikawa, L., 2005. Parallel adaptive numerical simulation of dry avalanches over natural terrain. J. Volcanol. Geotherm. Res. 139 (1–2), 1–21.

Patra, A., Bevilacqua, A., Akhavan-Safaei, A., Pitman, E.B., Bursik, M., Hyman, D., 2020. Comparative analysis of the structures and outcomes of geophysical flow models and modeling assumptions using uncertainty quantification. Front. Earth Sci. 8, 275.

Pepe, A., Calò, F., 2017. A Review of Interferometric Synthetic Aperture RADAR (InSAR) Multi-Track Approaches for the Retrieval of Earth's Surface Displacements. Appl. Sci. 7 (12), http://dx.doi.org/10.3390/app7121264.

Pinel, V., Hooper, A., De la Cruz-Reyna, S., Reyes-Davila, G., Doin, M., Bascou, P., 2011. The challenging retrieval of the displacement field from InSAR data for andesitic stratovolcanoes: Case study of Popocatepetl and Colima Volcano, Mexico. J. Volcanol. Geotherm. Res. 200 (1), 49–61. http://dx.doi.org/10.1016/j.jvolgeores.2010.12.002.

Pinel, V., Poland, M., Hooper, A., 2014. Volcanology: Lessons learned from Synthetic Aperture Radar imagery. J. Volcanol. Geotherm. Res. 289, http://dx.doi.org/10.1016/j.jvolgeores.2014.10.010.

Platz, T., Cronin, S.J., Procter, J.N., Neall, V.E., Foley, S.F., 2012. Non-explosive, dome-forming eruptions at Mt. Taranaki, New Zealand. Geomorphology 136 (1), 15–30, Publisher: Elsevier.

Pritchard, M., Ebmeier, S., Poland, M., Biggs, J., Hamling, I., Aoki, Y., Albino, F., Delgado, F., Dualeh, E., Grandin, R., 2021. Contrasting volcanic activity across Latin America, Southeast Asia, and Africa with multi-parameter satellite monitoring data: The CEOS Volcano Demonstrator. In: AGU Fall Meeting Abstracts. In: AGU Fall Meeting Abstracts, vol. 2021, pp. G24B–03.

Procter, J., Cronin, S.J., Fuller, I.C., Lube, G., Manville, V., 2010. Quantifying the geomorphic impacts of a lake-breakout lahar, Mount Ruapehu, New Zealand. Geology 38 (1), 67–70.

Procter, J., Cronin, S., Platz, T., Patra, A., Dalbey, K., Sheridan, M., Neall, V., 2009a. Mapping block-and-ash flow hazards based on Titan 2D simulations: A case study from Mt. Taranaki, NZ. Nat. Hazards 53, 483–501. http://dx.doi.org/10.1007/s11069-009-9440-x.

Procter, J.N., Cronin, S.J., Zernack, A.V., 2009b. Landscape and sedimentary response to catastrophic debris avalanches, western Taranaki, New Zealand. Sediment. Geol. 220 (3–4), 271–287, Publisher: Elsevier.

Procter, J., Cronin, S., Zernack, A., Lube, G., Stewart, R., Nemeth, K., Keys, H., 2014. Debris flow evolution and the activation of an explosive hydrothermal system; Te Maari, Tongariro, New Zealand. J. Volcanol. Geotherm. Res. 286, 303–316. http://dx.doi.org/10.1016/j.jvolgeores.2014.07.006.

Procter, J.N., Zernack, A.V., Cronin, S.J., 2021a. Computer Simulation of a Volcanic Debris Avalanche from Mt. Taranaki, New Zealand. In: Roverato, M., Dufresne, A., Procter, J. (Eds.), Volcanic Debris Avalanches: from Collapse To Hazard. Springer International Publishing, Cham, pp. 281–310. http://dx.doi.org/10.1007/978-3-030-57411-6_11.

Procter, J., Zernack, A., Mead, S., Morgan, M., Cronin, S., 2021b. A review of lahars; past deposits, historic events and present-day simulations from Mt. Ruapehu and Mt. Taranaki, New Zealand. N. Z. J. Geol. Geophys. 64 (2–3), 479–503. http://dx.doi.org/10.1080/00288306.2020.1824999.

Remy, D., Bonvalot, S., Briole, P., Murakami, M., 2003. Accurate measurements of tropospheric effects in volcanic areas from SAR interferometry data: application to Sakurajima volcano (Japan). Earth Planet. Sci. Lett. 213 (3), 299–310. http://dx.doi.org/10.1016/S0012-821X(03)00331-5.

Rosen, P., Hensley, S., Joughin, I., Li, F., Madsen, S., Rodriguez, E., Goldstein, R., 2000. Synthetic aperture radar interferometry. Proc. IEEE 88 (3), 333–382. http://dx.doi.org/10.1109/5.838084.

Simakov, N.A., Jones-Ivey, R.L., Akhavan-Safaei, A., Aghakhani, H., Jones, M.D., Patra, A.K., 2019. Modernizing Titan2D, a parallel AMR geophysical flow code to support multiple rheologies and extendability. Springer, pp. 101–112.

Stefanescu, E., Bursik, M., Dalbey, K., Jones, M., Patra, A., Pitman, E., 2010. DEM uncertainty and hazard analysis using a geophysical flow model.

Stefanescu, E., Bursik, M., Patra, A., 2012. Effect of digital elevation model on Mohr-Coulomb geophysical flow model output. Nat. Hazards 62, http://dx.doi.org/10.1007/s11069-012-0103-y.

Stevens, N., Manville, V., Heron, D., 2003. The sensitivity of a volcanic flow model to digital elevation model accuracy: experiments with digitised map contours and interferometric SAR at Ruapehu and Taranaki volcanoes, New Zealand. J. Volcanol. Geotherm. Res. 119 (1), 89–105. http://dx.doi.org/10.1016/S0377-0273(02)00307-4.

Tachikawa, T., Hato, M., Kaku, M., Iwasaki, A., 2011. Characteristics of ASTER GDEM version 2. In: 2011 IEEE International Geoscience and Remote Sensing Symposium. pp. 3657–3660. http://dx.doi.org/10.1109/IGARSS.2011.6050017.

Thiele, A., Dubois, C., Cadario, E., Hinz, S., 2013. Smart filtering of interferometric phases for enhancing building reconstruction. ISPRS - Int. Arch. Photogramm. Remote. Sens. Spat. Inf. Sci. XXXVIII-3/W22, 161–166. http://dx.doi.org/10.5194/isprsarchives-XXXVIII-3-W22-161-2011.

Tsokas, A., Rysz, M., Pardalos, P.M., Dipple, K., 2022. SAR data applications in earth observation: An overview. Expert Syst. Appl. 205, 117342.

Ui, T., Kawachi, S., Neall, V.E., 1986. Fragmentation of debris avalanche material during flowage—Evidence from the Pungarehu Formation, Mount Egmont, New Zealand. J. Volcanol. Geotherm. Res. 27 (3–4), 255–264.

Viotto, S., Toyos, G., Bookhagen, B., 2023. An assessment of the effects of DEM quality and spatial resolution on a model for mapping lahar inundation areas at volcán Copahue (Argentina & Chile). J. South Am. Earth Sci. 121, 104138. http://dx.doi.org/10.1016/j.jsames.2022.104138.

Weiss, A., 2001. Topographic position and landforms analysis.

White, L., Brisco, B., Dabboor, M., Schmitt, A., Pratt, A., 2015. A Collection of SAR Methodologies for Monitoring Wetlands. Remote. Sens. 7 (6), 7615–7645. http://dx.doi.org/10.3390/rs70607615.

Wilson, G., Wilson, T., Deligne, N., Cole, J., 2014. Volcanic hazard impacts to critical infrastructure: A review. J. Volcanol. Geotherm. Res. 286, 148–182. http://dx.doi.org/10.1016/j.jvolgeores.2014.08.030.

Woodhouse, I.H., 2005. Introduction to microwave remote sensing. CRC Press.

Yu, H., Lan, Y., Yuan, Z., Xu, J., Lee, H., 2019. Phase unwrapping in InSAR: A review. IEEE Geosci. Remote. Sens. Mag. 7 (1), 40–58.

Zernack, A.V., 2020. Volcanic debris-avalanche deposits in the context of volcaniclastic ring plain successions—a case study from Mt. Taranaki. In: Volcanic Debris Avalanches: From Collapse To Hazard. Springer, pp. 211–254.

Zernack, A., Cronin, S., Neall, V., Procter, J., 2011. A medial to distal volcaniclastic record of an andesite stratovolcano: detailed stratigraphy of the ring-plain succession of south-west Taranaki, New Zealand. Int. J. Earth Sci. 100 (8), 1937–1966.

Zernack, A.V., Procter, J.N., 2020. Cyclic growth and destruction of volcanoes. In: Volcanic Debris Avalanches: From Collapse To Hazard. Springer, pp. 311–355. http://dx.doi.org/10.1007/978-3-030-57411-6_12.

Zernack, A.V., Procter, J.N., Cronin, S.J., 2009. Sedimentary signatures of cyclic growth and destruction of stratovolcanoes: a case study from Mt. Taranaki, New Zealand. Sediment. Geol. 220 (3–4), 288–305.

Zhao, Z., Wu, Z., Zheng, Y., Ma, P., 2021. Recurrent neural networks for atmospheric noise removal from InSAR time series with missing values. ISPRS J. Photogramm. Remote Sens. 180, 227–237. http://dx.doi.org/10.1016/j.isprsjprs.2021.08.009.

Zhou, X., Chang, N.-B., Li, S., 2009. Applications of SAR interferometry in earth and environmental science research. Sensors 9 (3), 1876–1912, Publisher: Molecular Diversity Preservation International (MDPI).